Computers in Biology and Medicine 138 (2021) 104913

Contents lists available at ScienceDirect

Computers in Biology and Medicine

journal homepage: www.elsevier.com/locate/compbiomed

Simulated tissue growth in tetragonal lattices with mechanical stiffness tuned for bone tissue engineering

Amit M.E. Arefin *, Michael Lahowetz, Paul F. Egan

Department of Mechanical Engineering, Texas Tech University, Lubbock, TX, 79409, USA

ARTICLE INFO

Keywords:
Tissue engineering
Scaffolds
Lattices
Simulations
Tissue growth
Elastic modulus

ABSTRACT

Bone tissue engineering approaches have recently begun considering 3D printed lattices as viable scaffold solutions due to their highly tunable geometries and mechanical efficiency. However, scaffold design remains challenging due to the numerous biological and mechanical trade-offs related to lattice geometry. Here, we investigate novel tetragonal unit cell designs by independently adjusting unit cell height and width to find scaffolds with improved tissue growth while maintaining suitable scaffold mechanical properties for bone tissue engineering. Lattice tissue growth behavior is evaluated using a curvature-based growth model while elastic modulus is evaluated with finite element analysis. Computationally efficient modeling approaches are implemented to facilitate bulk analysis of lattice design trade-offs using design maps for biological and mechanical functionalities in relation to unit cell height and width for two contrasting unit cell topologies. Newly designed tetragonal lattices demonstrate higher tissue growth per unit volume and advantageous stiffness in preferred directions compared to cubically symmetric unit cells. When lattice beam diameter is fixed to 200 μm, Tetra and BC-Tetra lattices with elastic moduli of 200 MPa–400 MPa are compared for squashed, cubic, and stretched topologies. Squashed Tetra lattices demonstrated higher growth rates and growth densities compared to symmetrically cubic lattices. BC-Tetra lattices with the same range of elastic moduli show squashed lattices tend to achieve higher growth rates, whereas stretched lattices promote higher growth density. The results suggest tetragonal unit cells provide favorable properties for biological and mechanical tailoring, therefore enabling new strategies for diverse patient needs and applications in regenerative medicine.

1. Introduction

3D printing enables the design of complex geometries that are tunable to support improved bone tissue growth with suitable mechanical stiffness [1–4]. Bone tissue engineering relies on implanting scaffold structures to regenerate tissue, which is necessary for spinal fusions and bone fractures that would otherwise not heal, and improve upon bone grafting operations used for 2.5 million people per year in the US and EU [5]. Despite recent efforts in bone scaffold design, clinical implementation of scaffolds remains limited due to a lack of understanding of how alterations in 3D printed scaffold configuration influence biological tissue growth and mechanical stiffness [6]. Issues that emerge from a lack of tissue growth and mechanical stiffness are partial bone regeneration from poor biomechanical signaling and potential mechanical failures [7]. Generally, scientific investigations for 3D printed tissue scaffolds have focused either on biological or mechanical functionality in isolation with symmetric unit cell structures, thereby only partially optimizing the scaffold [8–13]. Improving scaffold tissue growth and mechanical stiffness often require opposing design alterations, particularly when considering the geometrical design of scaffolds [14], since scaffold geometry influences local curvature that drives tissue growth and stress distributions [15,16]. Here, we consider scaffolds with asymmetric unit cell designs that enable tailoring of tissue growth and mechanical stiffness according to *in vivo* loading. Proposed designs are assessed in the context of spinal fusion, where a scaffold is implanted between vertebrae and subjected to axial loading F_z (Fig. 1).

Spinal fusion treatments consist of implanting a scaffold with specified stiffness and porosity to promote the fusion of adjacent vertebrae [17,18]. 3D printed tissue scaffolds have been investigated as a means for improving fusion treatments because they enable mechanical efficiency, high nutrient transport, and personalized design configurations [19,20]. Recent approaches have used 3D printed demineralized bone matrix and metamaterial titanium scaffolds [21,22], however, these types of scaffolds are limited in terms of topological

* Corresponding author.
E-mail address: amit.arefin@ttu.edu (A.M.E. Arefin).

https://doi.org/10.1016/j.compbiomed.2021.104913
Received 5 June 2021; Received in revised form 12 September 2021; Accepted 27 September 2021
Available online 1 October 2021

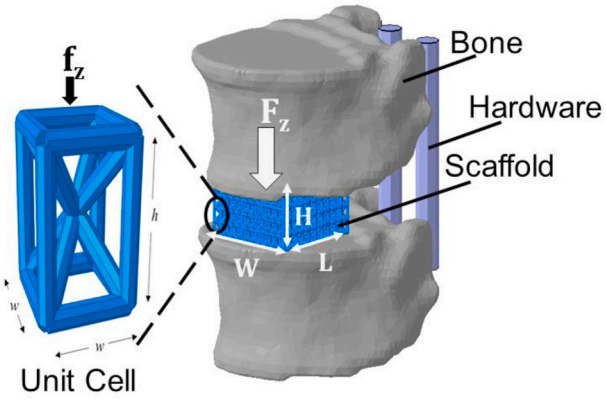

Fig. 1. Scaffold lattice designed for spinal fusion. Design approach demonstrating tetragonal unit cell patterned to form a scaffold implanted in spine between two vertebrae, with spinal axial load F_z that is experienced as load f_z for each unit cell. Key design parameters are also indicated.

complexity/resolution or suitable material stiffness that can be achieved by polymer 3D printing for scaffolds [23]. The primary load experienced by the scaffold is the axial load F_z of the spine, that is distributed to each unit cell as f_z. The unit cells patterned to form a metamaterial lattice inform the overall stiffness of the scaffold, where the effective elastic modulus of the unit cell is representative of the effective elastic modulus of the scaffold. Supporting vertebral fusion hardware will also result in modulation of forces experienced by the scaffold that enables further optimization of the mechanical functionality of the system.

Many lattice design approaches have been artificially limited by focusing on lattices with cubic unit cell symmetry that provide simplicity for conducting experiments and fabrication while retaining the benefits of an architected material's mechanical efficiency for strength per relative density [24]. Lattices are typically configured as scaffolds with porosities of 50%–80% necessary to facilitate voluminous tissue growth. Cubic unit cell symmetry limits lattices to have the same properties in all directions despite biomechanical loadings often occurring in aligned directions in tissue engineering sites [25]. Therefore, tetragonal unit cells for lattices that modify cubic unit cells by introducing a design parameter to alter unit cell height independently of unit cell length/width, as communicated in Fig. 1, could provide an improvement over the cubic unit cell symmetry found in commonly used tissue scaffold designs.

Specifically, the mechanical property of effective elastic modulus can be tuned along different axes of the unit cell, therefore facilitating design tailoring for *in vivo* loading cases where loading on the scaffold is has a tailored stiffness response [3,26,27]. The mechanical simulation in the current study is conducted using finite element analysis [25]. The simulation predicts elastic moduli based on unit cell topology and beam directionality throughout a lattice [28]. The simulation is amenable to predicting properties of tetragonal structures since adjusting the height of unit cells alters elastic moduli for varied loading directions. The finite element simulations are used to understand the effective properties of the lattice as a metamaterial, since the lattice is expected to retain scalable structure properties when patterned as a larger lattice to fit constraints of an injury site when implanted [29]. Finite element simulations for 3D printed structures have been well validated with experimental studies, and state of the art polymer 3D printed scaffolds have suitable stiffness for spinal fusion applications. The stiffness of polymer scaffolds is advantageous over commonly used titanium scaffolds because they better match the effective elastic modulus of trabecular bone, which mitigates stress shielding that can lead to lower density bone growth. Additionally, polymer scaffolds degrade in the body over time which reduces risk if further complications occur after the initial surgery.

Although tetragonal configurations enable mechanical tailoring, it is less obvious how they affect biological functionality, which includes processes for tissue growth, vascularization, and nutrient transport [30–32]. Here, we focus on the growth of the tissue itself, as it is the primary biological functionality for scaffolds and is dependent directly on the design of the scaffold. Tissue growth is primarily driven by the geometry of the scaffold [33,34], and when considering tissue-growth on complex surfaces, such as 3D printed lattices, is difficult to predict based on the geometry of the lattice alone, thereby necessitating numerical or simulation approaches for evaluation. There are several methods for predicting tissue growth informed by biological experiments that include surface tension [35], curvature-based growth [36], mechanobiological algorithms [37], continuum tissue growth [38], and agent-based growth models [39]. Mechanical stimulation is not typically included in many modeling approaches to avoid model complexity and to gain time-efficiency when evaluating on the basis of scaffold geometry alone [40,41], which is particularly important when considering a large number of design alternatives. Recent simulations in curvature-based tissue growth have been adopted as an efficient means of evaluating 3D printed scaffolds [42]. Results have demonstrated cubic lattices have halted tissue growth, meaning tissue growth stops and only partially regenerates tissue to fill the scaffold porous volume. Investigation of tetragonal lattices therefore presents an opportunity to improve upon these designs, by introducing further planar pore sizes/-shapes for a single unit cell. These design decisions enable bridging of tissues to fill smaller pore shapes to avoid scenarios of tissue growth halting due to lack of concave curvature initially found in beam-based lattices [12], which can be evaluated through investigations with curvature-driven growth models.

There has been much work to validate curvature-based tissue growth models with both *in vitro* and *in vivo* experimentation that motivates the use of computational methods to investigate novel scaffold designs and evaluate them at a much faster rate than possible through further resource-intensive experiments [43]. Linear tension driving tissue growth has been studied in simple pore shapes, relating substrate geometry to curved tissue fronts [44]. A voxel-based simulation environment was then developed to study curvature-driven growth on complex surfaces that led to initial quantified predictions for how the scaffold geometry drives tissue growth [45]. In simple 2D pores, substrate geometry plays a minimal role in quantified differences relating to shape optimization [46], but 3D printed structures with open pores lead to a much more complex set of trade-offs [12]. Differences in pore size for 3D printed scaffolds have been evaluated for titanium scaffolds of different shapes and validated with *in vitro* studies with subsequent numerical simulations agreeing with the experiments [47]. Further efforts demonstrated how curvature-driven growth is affected by fluid transport related to nutrient availability, however, these lead to highly expensive simulations for investigating limited scaffold design decisions in relation to tissue growth [47]. A more recent effort has demonstrated curvature-based tissue growth simulations corresponding to *in vivo* bovine bone growth [36] and further *in vitro* studies demonstrating the exponential increase in tissue growth time with larger pores [35]. The large body of evidence supporting curvature-based growth models with empirical validation, and their recent use for efficient evaluation of tissue growth on 3D printed structures, situates the approach well for bulk investigation of 3D printed scaffolds with novel topologies.

Once simulations are completed, there is a need to compare designs to determine which scaffolds are most promising for bone tissue engineering, which is challenging since biological and mechanical scaffold requirements are often conflicting. Mechanical and biological simulation results are investigated for tunable lattices in this study by parametric sweeping of design parameters describing a lattice's unit cell dimensions which are later used to create design maps to investigate how multiple independent parameters influence specific scaffold properties such as tissue growth rates or elastic modulus. Design maps have recently been used as a means to compare scaffolds based on tissue

growth [12], where scaffolds had increased growth with increased surface-volume ratio and topology dependency. Elastic modulus and manufacturability have been used in design maps for titanium structures with octet unit cells to find suitable stiffness for scaffolds that additionally resulted in tissue growth [48,49]. Design mapping requires computationally efficient models to conduct bulk analysis that provides high numbers of evaluations to select candidate designs that could later be investigated more in-depth for specific application requirements that drive design selection. After design selection, lattice fabrication is possible with stereolithography 3D printing using biocompatible materials, which demonstrates the feasibility of printing these types of structures for clinical tissue engineering applications [50].

The goal of this paper is to investigate a novel approach for tuning tetragonal unit cells by altering unit cell height to form squashed/stretched unit cell geometries that result in improved tissue growth rate/volume while retaining suitable mechanical stiffness for bone tissue engineering. Investigations conducted in this paper benefit from computational exploration of controlled alterations of lattice structures at a much faster rate than experiments. Tetragonal lattices are compared to lattices with cubic unit cell symmetry as a control, by generating lattices with porosities suitable for bone tissue engineering. Tissue growth simulations and finite element analysis are conducted to provide insight into the behavior of tetragonal scaffolds in comparison to the control condition, followed by a mapping of the design space. These investigations enable the discovery and justification of potentially high-performing scaffold designs enabled by tetragonal unit cell configurations that are suitable for bone fusion and provide capabilities surpassing those of conventional lattice designs. This study is a stepping stone towards understanding and optimizing the trade-offs of biological and mechanical functionalities with computational engineering design methodologies in personalized medicine, and could promote the discovery of advantageous strategies for configuring lattices on a patient-specific basis using 3D printing.

2. Design and simulation methods

2.1. Computational methodology

A flowchart is presented in Fig. 2 that demonstrates the computational methodology for carrying out work to evaluate tetragonal unit cell lattices and aid design selection based on their tissue growth behavior and mechanical stiffness relevant to spinal fusion applications. There are four phases identified for the flow chart: (1) Design generation of parametrically altered tetragonal structures, (2) Simulations to evaluate tissue growth and mechanical properties, (3) Mapping of designs based on their evaluated outputs, and (4) Assessing trade-offs and selecting designs according to constraints imposed by the bone fusion application.

2.2. Structural design

Scaffolds are designed with tetragonal lattice structures, according to Bravais lattice structure topological connections that have one parameter h describing the unit cell height and one parameter w describing the width of the unit cell that describes lengths of its square planar base (Fig. 3). Structures were generated using a python script that specified Abaqus (version 6.19–1) to arrange beams to form unit cells that are then patterned to form a lattice.

The first topology considered is a simple tetragonal (referred to as Tetra) configuration of a unit cell that has beams arranged on each unit cell edge (Fig. 3A). The second unit cell topology is a body-centered tetragonal (referred to as BC-Tetra) unit cell that has beams arranged on each unit cell edge and one beam from each unit cell corner to the volumetric center (Fig. 3B). According to the definition used here, cubic unit cell structures (e.g. Cube and BC-Cube) are special cases of tetragonal structures (e.g. Tetra and BC-Tetra) when height is equal to width, meaning all Cube and BC-Cube unit cells are specific cases of Tetra and BC-Tetra unit cells that have cubic symmetry. All unit cell beams generated have circular cross-sections with a diameter of 200 μm, which is representative of beam diameters that facilitate tissue growth and are achievable with 3D printing processes.

2.3. Tissue growth simulation

The curvature-based tissue growth simulation for the tetragonal structures is adapted from past approaches and implemented in a voxel-based environment [12] and well-validated experimentally *in vitro* and

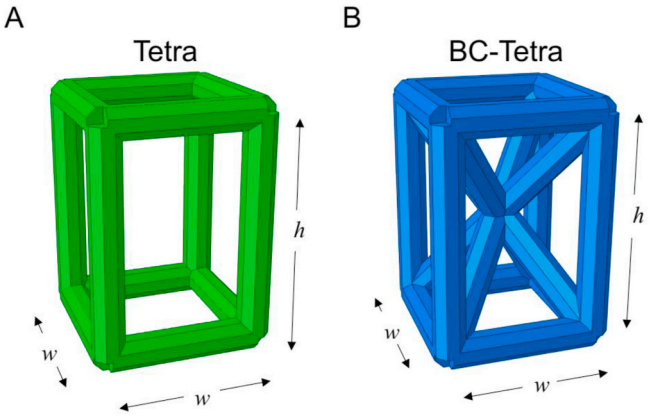

Fig. 3. Tetragonal unit cell design parameterizations. Designs consist of a A) Tetra unit cell and B) BC-Tetra unit cell with parameters describing unit cell height h and width w. Images exported from Abaqus.

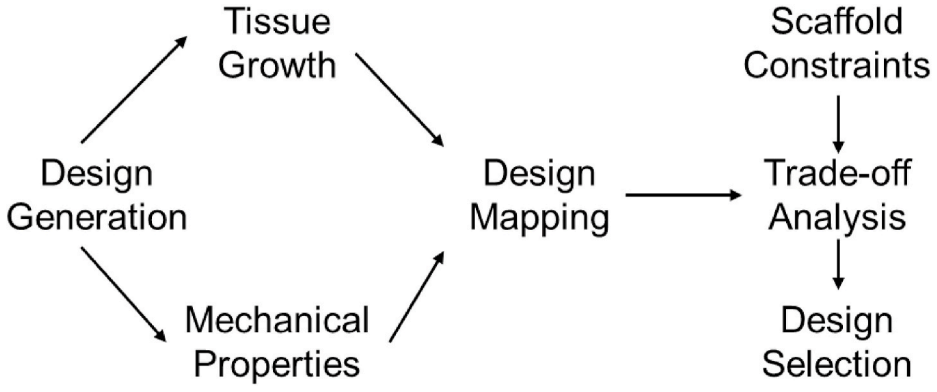

Fig. 2. Flowchart demonstrating computational design approach. Steps include (1) Parametric deign generation, (2) Simulation for tissue growth and mechanical properties, (3) Parametric design mapping of simulation results, and (4) Design selection according to trade-off analysis for scaffold constraints.

in vivo [35,36]. Here, a brief description of the curvature-based tissue growth simulation is provided with highlights for alterations to the method for implementation with tetragonal unit cell structures that was implemented using python code in a three-dimensional voxel environment. The python code was modified from previous efforts to enable the generation and simulation of tetragonal structures that have unit cell height-adjustable independently of unit cell width. The voxel environment was visualized in ParaView (version 5.6.0) by reading.csv files specifying the voxel location and state throughout the environment at each time step of the simulation. Unit cell designs were created in a virtual environment that consists of four types of voxels that represent the structure, tissue, interface, and void volume, as demonstrated in Fig. 4.

In Fig. 4 structure voxels represent the 3D printed lattice volume. Tissue voxels represent deposited tissue that includes the initially seeded tissue on the structure or newly grown tissue throughout the simulation. Interface voxels represent the tissue growth front where new tissue may grow if local curvature is positive (i.e. concave). Void voxels represent space where tissue may eventually grow. The virtual environment has a height of $h/2$, where h is the height of a unit cell and a width of $w/2$ where w is the width of a unit cell. Beams are generated to form unit cell topologies by placing structure voxels in the environment according to a specified configuration. Only one-eighth of a unit cell is constructed to reduce the computational cost of each simulation. The behavior of growth at the boundaries of the virtual environment is mirrored during simulations which assumes symmetrical unit cells are replicated to form a continuous lattice structure.

The virtual environment is created by placing structure voxels to form a structure based on specified design parameters. Tissue voxels are placed adjacent to the structure voxels to represent initial seeded tissue on the structure. Interface voxels are placed adjacent to the tissue voxels to represent the boundary between the void space and advancing tissue front. The ratio of the volume of solid structure/tissue and the volume of void space concerning each interface voxel is calculated with a spherical scanning mask. Mask radius m_r dictates the voxel length ds according to

$$ds = \frac{c_r}{m_r} \tag{1}$$

The parameter c_r represents the reach of cells to mechanically sense their environment. According to previous curvature-based models, cell reach c_r is held at a constant 55 μm and 5.5 voxels is a suitable mask radius for most cases to ensure accurate/consistent simulation, therefore defining the voxel length ds as 10 μm [51,52]. A higher mask radius improves the resolution of the simulation which requires more computational time for evaluation and in some cases improves accuracy/consistency of simulations results. If the number of voxels making up the mask increases, then the voxels represent a smaller distance in the virtual environment due to the constant physical constraint of the cell reach based on osteoblast size. The voxel representation for the scanning mask is demonstrated in Fig. 4 that has a diameter equal to $2{\cdot}m_r$ and is applied to interface voxels each step of the simulation. Therefore, increasing the mask radius also increases the computational time required for the simulation and has diminishing returns on accuracy, thereby motivating the use of the smallest mask size that returns consist results, which was determined as 6.5 voxel radius.

In every simulation step, the scanning mask calculates the local curvature, κ for each interface voxel according to the following equation for voxels present in a single scanning mask:

$$\kappa = \frac{16}{3\,.\,c_r}\left(\frac{m_{on}}{m_{on}+m_{off}} - \frac{1}{2}\right) \tag{2}$$

The scanning mask is applied to each interface voxel during the simulation where the type of each voxel within the mask is counted to determine m_{on} and m_{off}. In equation (2), m_{on} represents the number of voxels that are not void (either structure voxel or tissue voxel) and m_{off} represents void voxels (either void voxel or interface voxel). The total number of voxels ($m_{on} + m_{off}$) making up the scanning mask is constant throughout the simulation, however, m_{on} and m_{off} are local variables that are determined based on distribution of different voxels within the scanning mask each time curvature is calculated. If local curvature is positive, it means there is a greater number of structure/tissue voxels in the mask than void/interface voxels, and therefore $m_{on} > m_{off}$. The equation determines if the curvature is concave and therefore positive when more than half of the voxels in the scanning masks are counted for by m_{on}. When scanning interface voxels, if κ is positive the curvature is concave and the interface voxel turns into the tissue for the next step, but if κ is non-positive (zero or negative), it remains an interface voxel for the next simulation step.

Tissue growth behavior is tracked at the initial simulation step once the tissue is seeded and calculated each subsequent step. Measured design properties and behaviors for evaluation are scaffold porosity P, tissue growth density g_d, and tissue growth rate g_r.

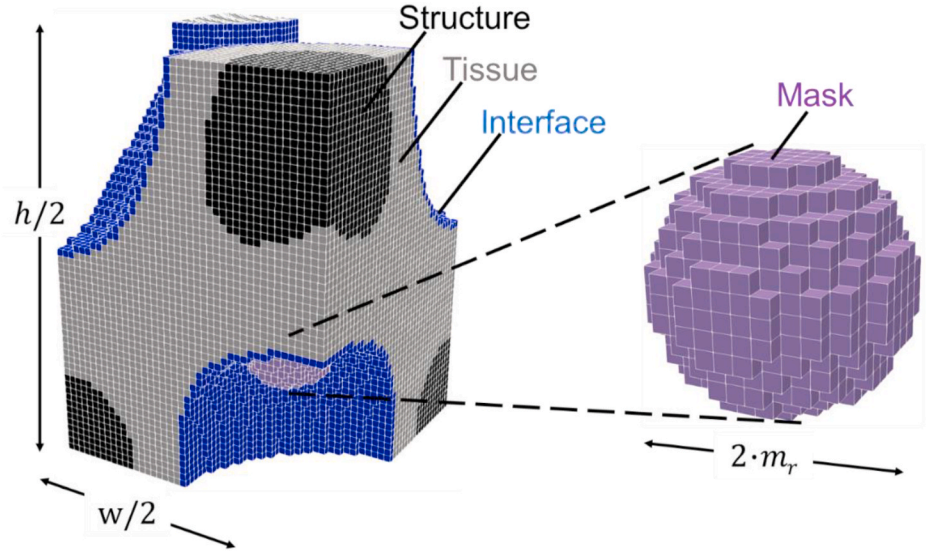

Fig. 4. Tissue Growth Simulation. A) Voxel environment for one-eighth of a Tetra-BC unit cell with height h and width w with simulated tissue growth. Voxels represent structure, tissue, and interface voxels in addition to the void voxels in the scanning mask. B) Voxels making up scanning mask with radius m_r. Images exported from ParaView.

All the voxels in the environment are tracked to calculate the porosity of the scaffold over time. The ratio of the number of void and interface voxels in the environment to the total number of voxels in the environment are used to calculate the porosity:

$$P = \frac{v_{void} + v_{interface}}{v_{total}} \tag{3}$$

here, P is the porosity, v_{void} is the void-volume measured by the number of void voxels, $v_{interface}$ is the void-volume measured by the number of interface voxels and v_{total} is the volume of the total environment measured by the total number of voxels in the environment.

The tissue growth density g_d is the ratio of the volume of tissue to the volume of the environment and is calculated by counting the number of tissue voxels and comparing to the total number of voxels:

$$g_d = \frac{v_{tissue}}{v_{total}} \tag{4}$$

with v_{tissue} as the tissue volume. The tissue growth rate g_r is the tissue growth density per unit time step:

$$g_r = \frac{g_d}{t} \tag{5}$$

where t is the total number of time steps required for the growth. The time step value is taken when the simulation converges, whether it is from complete or halted void filling behavior. Convergence occurs when there are no remaining interface voxels with positive curvature.

2.4. Mechanical stiffness simulation

A finite element analysis with beam elements is used to calculate the elastic modulus of the designed lattice structures. Abaqus software is implemented using python scripting to generate beams patterned as unit cells and then organized to form a lattice structure [25]. Each structure has 27 unit cells in a $3 \times 3 \times 3$ patterning. The relative elastic modulus is calculated by determining the ratio between the effective elastic modulus of the lattice compared to the elastic modulus of the base material used to construct the lattice [53]. When standard biocompatible polymers such as polylactic acid or methacrylic acid are considered as the base material, their elastic modulus is estimated as 2000 MPa [54]. The mechanical response of the lattice is approximated from a quadratic finite element analysis based on the Euler-Bernoulli beam theorem that is carried out using the python script to automate evaluations in Abaqus. Each beam in the evaluation was sub-divided into three finite elements. All evaluations assumed linear elastic material behavior. Data is output that details the relative elastic modulus of the structure that is used to map mechanical properties in relation to the specified design configuration. Fig. 5 shows the boundary conditions of the simulation.

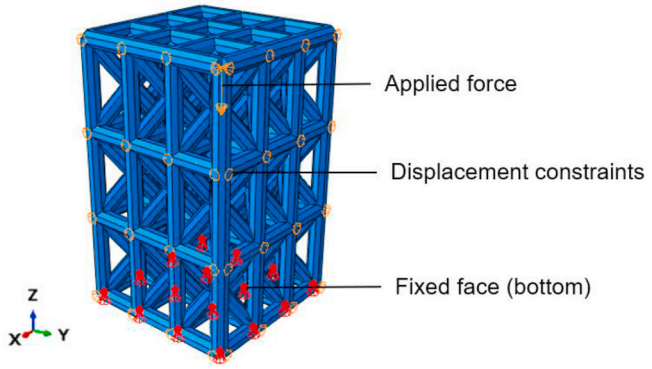

Fig. 5. Boundary conditions of the mechanical simulation. Each lattice is subject to an applied force distributed across one z-plane face with opposing face fixed. Constraints impede displacement for faces on x and y-planes and impede rotation. Images exported from Abaqus.

The boundary conditions are selected to represent a uniaxial loading case for compression, similar to compression loading in the spine or mechanical testing compression experiments and constrained to mitigate rotation to provide a measure of the effective elastic modulus. The simulation is conducted by applying a unidirectional displacement δ equal to 1% of the lattice height to the nodes on the face of the lattice perpendicular to a face with fixed displacement. The simulation calculates the displacement used to calculate the longitudinal effective elastic modulus E_z of the lattice with the following equation:

$$E_z = \frac{F_z}{A_z} \cdot \frac{H}{\delta_z} \tag{6}$$

here, F_z is the reaction force in z direction, H is the scaffold height (aligned parallelly with z direction), A_z is the area of the scaffold surface perpendicular to the displacement (i.e. perpendicular to z direction), δ_z is height displacement is assumed as $\delta_z = 0.01h$.

The effective transverse elastic modulus $E_x$in the x-direction uses the following equation:

$$E_x = \frac{F_x}{A_x} \cdot \frac{w}{\delta_x} \tag{7}$$

here, F_x is the reaction force in x direction, w is the scaffold width (aligned parallelly with x direction), A_x is the area of the scaffold surface perpendicular to the displacement (i.e. perpendicular to x direction), δ_x is width displacement assumed as $\delta_x = 0.01w$. Here, the boundary conditions from Fig. 5 are changed so that the displacement in the x-direction of the lattice is fixed (rather than z) and the loading is perpendicular to this fixed face. Since the width and length of the lattice are the same in all configurations, it is assumed E_y is equivalent to E_x.

3. Results

3.1. Design generation

Design maps are first generated to determine how the independent design parameters of unit cell height and width affect scaffold porosity. The map is created by calculating the porosity of the scaffold before cell seeding for Tetra and BC-Tetra unit cells. Porosity is calculated by comparing the ratio of void voxels to the total number of voxels for each generated structure. Fig. 6 shows the porosity map for the Tetra structure with the unit cell height and width ranging from 300 μm to 800 μm in 50 μm increments.

The porosity of the Tetra lattices in Fig. 6A ranges from 33% to 86%. The design map shows that as both height and width increase the porosity increases, due to the larger pore sizes created in the scaffold as unit cell size becomes larger relative to the fixed diameter beams. There is a nonlinear relationship between porosity and the independent design parameters, which is evidenced by the concave curves of constant porosity present on the map, which is highlighted for porosities of 50% and 70%.

For the BC-Tetra structure, porosity is mapped as height and width are swept from 500 μm to 1500 μm in 100 μm increments (Fig. 6B). The porosity ranges in Fig. 6B from 29% to 88%. The design map shows that porosity increases as height and width increase, with a similar nonlinear relationship to the Tetra unit cells. However, since Tetra unit cells do not have diagonal beams present in BC-Tetra unit cells, the Tetra design achieves the same porosity as the BC-Tetra unit cell at a smaller unit cell size. For instance, at 50% porosity, the Tetra unit cell having a height of 600 μm has a width of 310 μm while the BC-Tetra unit cell having the same height of 600 μm has a width of 690 μm. Designs are present in the 50%–80% range of porosity suitable for bone tissue engineering for both topologies and are therefore valid structures for continued analysis for investigating behaviors in trade-offs with biological and mechanical

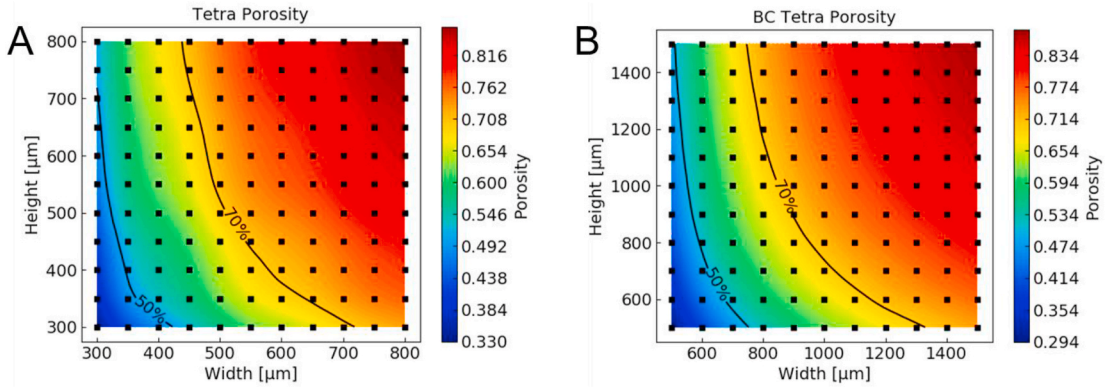

Fig. 6. Porosity maps for Tetra and BC-Tetra lattices. Unit cell height and width are altered as independent variables as porosity is determined and plotted. The lines inside the map indicate design configurations that all have porosities of 50% of 70% along the line. Each plotted data point represents a unique design with porosity calculated to generate the map.

simulations.

3.2. Tissue growth simulations

Biological behaviors of unit cells are investigated by comparing tetragonal lattices to cubic lattices with controlled design parameters and porosity values. Differences in tissue growth are expected to occur due to tetragonal lattices introducing planar pores with higher/lower aspect ratios than present in cubic lattices. These comparisons are conducted by first generating a 42% porous cubic Tetra unit cell with equal unit cell height and width of 350 μm that demonstrates complete void filling behavior in 29 time steps, then increasing Tetra unit cell height and width to 440 μm for a porosity 55% when tissue growth halts at 28 time steps, therefore resulting in partial void filling behavior. A stretched Tetra unit cell is then generated by extending the height to 660 μm but keeping the 350 μm width of the first structure as to reach the 55% porosity of the second structure and retains complete void filling behavior with convergence at a time step of 77, as demonstrated in Fig. 7 with simulation renderings at key time steps in Fig. 8.

Figs. 7 and 8 show how tissue grows in the simulated configurations from initial seeding to the final time step when the last structure has converged. It is observed that a stretched Tetra lattice avoids halted growth if one of its pores closes to provide a continued curved surface throughout the entire simulation. All the pores in the small cubic configuration close at the same time, whereas the larger cubic configuration has halted tissue growth as the pores remain open. The stretched Tetra configuration shows its square pore close early in the simulation that ensures complete void filling behavior.

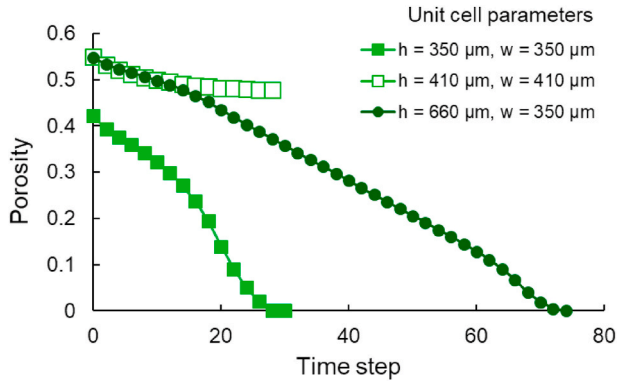

Fig. 7. Tissue growth simulation for Tetra lattices. Change in porosity per time step as tissue fills void space for lattices with unit cells of height h and width w.

Next, the tissue growth for controlled comparison of a squashed BC-Tetra structure was investigated and compared to BC-Tetra structures with cubic configurations. For the first sample design of the BC-Tetra topology, a cubic unit cell height of 700 μm is selected along with an equal width, which gives an initial porosity of 52% that has complete void filling behavior in 59 time steps. The height and width of this cubic unit cell is then increased to 900 μm to provide an initial porosity of 68% with partial void filling behavior that halts at a time step of 191. Next, a squashed BC-Tetra design was generated by setting its height to that of the smaller cubic structure of 700 μm and expanding its width to 1050 μm until it reaches 68% porosity equal to the larger cubic structure. This squashed BC-Tetra has complete void filling behavior at time step of 289, with results for all unit cells demonstrated as a growth vs time-step plot in Fig. 9 and with simulation renderings at key time steps in Fig. 10.

Figs. 9 and 10 show how tissue grows in the selected configurations. The figures demonstrate that a squashed tetragonal lattice avoids halted growth because it reaches a point where the smallest inner pore closes between prior to time step 160. The closing of the smaller pore in this squashed BC-Tetra design and the smaller cubic BC-Tetra design provides a concave curved surface for sustained growth whereas growth halts for the larger cubic BC-Tetra design.

When considering both the Tetra and BC-Tetra cases results demonstrate it is possible to generate a height-adjusted design that is either stretched or squashed with complete void filling behavior at a higher porosity than is possible with cubic configurations. Therefore, the tetragonal lattice topologies with non-equal height and width achieve higher tissue growth density since they provide more tissue growth for a given porosity than cubic unit cells with equal height and width.

3.3. Mechanical property simulations

Simulations were conducted to investigate the mechanical behavior of height-adjusted tetragonal lattices in comparison to cubic tetragonal lattices and determine their elastic moduli. Finite element analysis is conducted in Fig. 11 for two Tetra lattice structures of equal 62% porosity, with the first cubic structure having a unit cell height and width of 450 μm and a second stretched Tetra unit cell with a unit cell height of 800 μm and a unit cell width of 350 μm.

Fig. 11 results demonstrate that loads are carried along members aligned with the loading direction, whereas orthogonal members do not carry loads. Both structures reach the same maximum Von Mises stress of 1.99 *MPa* although their effective elastic moduli differ. The cubic Tetra structure has an effective longitudinal elastic modulus of 480 *MPa* while the stretched Tetra structure has a higher effective longitudinal elastic modulus value of 697 *MPa*.

The finite element analysis is then conducted with BC-Tetra lattice structures with cubic and stretched unit cell configurations. The cubic

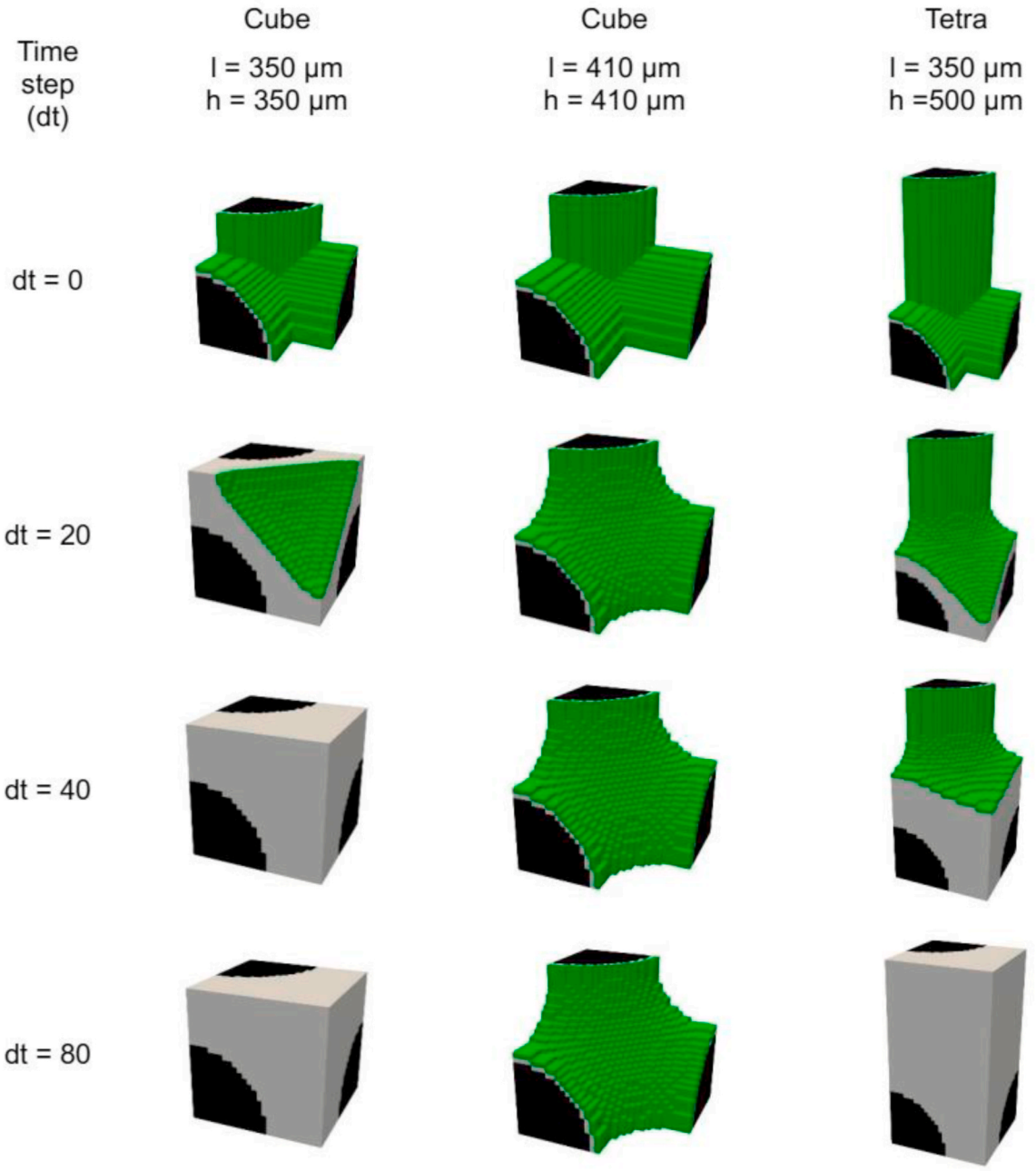

Fig. 8. Simulation rendering demonstrating tissue filling behavior of Tetra lattices. Voxels represent structure (black), tissue (gray), interface (green). Tissue voxels replace interface voxels with positive curvature each time step. Images exported from Paraview.

BC-Tetra structure has a unit cell height and width of 700 μm that makes it 60% porous and the stretched BC-Tetra structure has a unit cell height of 1500 μm unit cell and width of 600 μm with an equivalent 60% porosity to the cubic configuration. Simulation results are presented in Fig. 12.

Results demonstrate a maximum Von-Mises stress of 2.05 MPa in the cubic BC-Tetra structure and lower maximum stress of 1.4 MPa. In the stretched BC-Tetra structure. In both structures, stress is highest for members along the loading direction but also some load is carried by diagonal members. As the height increases for the BC-Tetra structure, the inner beams (body-centered beams) become more aligned towards the loading direction in the z-axis and carry a larger proportion of the loading, thereby leading to lower maximum stress in the stretched BC-Tetra structure. These differences are also observed by an effective elastic modulus of 11.77 MPa for the cubic BC-Tetra structure, compared to a higher effective elastic modulus of 29.23 MPa for the stretched BC-Tetra structure.

3.4. Design mapping

Biological and mechanical simulations were conducted for all the designs evaluated in Fig. 6 are mapped using height and width as independent parameters. Fig. 13 shows the results for four design maps of the Tetra lattice topology, with maps generated for tissue growth density, tissue growth rate, longitudinal elastic modulus, and transverse elastic modulus.

Tissue growth density from Fig. 13A demonstrates when the height and width of the unit cell are equal for cubic configurations that further increases to height/width results in tissue growth density increases until tissue growth behavior halts at a unit cell height/width of 400 μm.

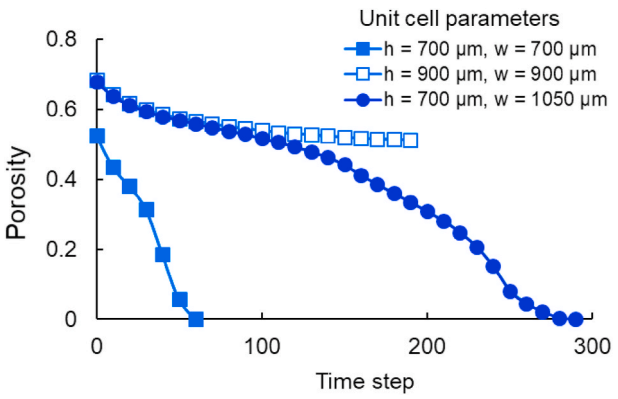

Fig. 9. Tissue growth simulation for BC-Tetra lattices. Change in porosity per time step as tissue fills void space for lattices with unit cells of height *h* and width *w*.

However, increasing height or width while setting the other equal to 350 μm results in complete void filling behavior with greater tissue growth density for higher values. The highest tissue growth density for cubic unit cells with equal height and width is 48%, whereas lattices with increased height achieve tissue growth density as high as 80%. Fig. 13B demonstrates that tissue growth rate is highest for smaller height and widths, but decreases significantly once scaffolds reach a porosity higher than 50%, with a range from 0.033 dt^{-1} to 0.002 dt^{-1} when considering the full map. Fig. 13C demonstrates the longitudinal elastic modulus which is elastic modulus along the *z*-axis that demonstrates a decrease in elastic modulus as width increases, however it remains nearly constant for all values of height. The consistency with height occurs because regardless of the height of the structure the same loads are carried with proportional displacement, whereas for width alterations the displacement remains constant while the dimensions of the structure increase, thereby decreasing elastic modulus according to equation (6). Fig. 13D demonstrates the transverse elastic modulus which is elastic modulus along the *x*-axis that follows a similar trend to tissue growth rate, such that the transverse elastic modulus decreases for larger unit cells from 1000 *MPa* to 160 *MPa* when considering the highest and lowest values on the map.

Design maps were also created for the BC-Tetra lattice topology by using height and width as independent parameters and covering larger unit cell structures compared to the Tetra lattices to ensure suitable porosities for tissue engineering are evaluated. Results are demonstrated in Fig. 14 for outputs of tissue growth density, tissue growth rate, longitudinal elastic modulus, and transverse elastic modulus.

In the tissue growth density map of Fig. 14A, tissue growth increases for higher heights and widths until halting occurs when void filling behavior no longer occurs. In the map, the highest tissue growth density for unit cells with equal height and width is around 64%, whereas stretched BC-Tetra unit cells with increased height achieve tissue growth density as high as 81%. In contrast to Tetra unit cells, the BC-Tetra unit cells have void filling behavior that creates a curved interface on the map, as opposed to the constant height/width lines for the Tetra structures. Fig. 14B demonstrates the tissue growth has similar behavior to Tetra unit cells in that it decreases for higher heights and widths. The longitudinal elastic modulus for BC-Tetra unit cells in Fig. 14C demonstrates different behavior than those of Tetra unit cells, with longitudinal elastic modulus increasing with height and decreasing with width. The increase in height occurs because greater stretching of BC-Tetra unit cells results in a higher proportion of diagonal beams aligned with the loading direction. The transverse elastic modulus in Fig. 14D demonstrates similar behavior to Tetra unit cells, such that increasing the height or width of the unit cell decreases the elastic modulus. These results demonstrate the relationships of biological and mechanical behaviors to the parametric design of Tetra and BC-Tetra unit cells and how each unit cell type enables different ways of manipulating design parameters to achieve desired behaviors and property trade-offs. The biological maps show that tetragonal unit cells help in achieving higher growth density that was not achievable with cubic unit cells, whereas mechanical maps show that tetragonal unit cells add more flexibility over elastic modulus tuning.

3.5. Scaffold trade-offs

Based on trends from design maps, tetragonal lattices of both topologies enable tailoring for property trade-offs according to a given application. However, only a subset of these lattices has specified properties appropriate for bone tissue engineering, which is considered by constraining the longitudinal elastic modulus in the range of 200 MPa–400 MPa that is appropriate for spinal fusion applications [55]. All the designs considered in the previous design maps fall within this range of longitudinal elastic modulus when plotted for growth rate vs growth density comparison in Fig. 15.

Fig. 15 demonstrates that each plot has a low growth density-low growth rate region being produced because of halted tissue growth, which represents the cluster of data points in the bottom left portion of each plot. Each plot has another region that includes high growth density-high growth rate lattices. This high growth density-high growth rate region indicates that there is a trade-off between the growth rate and growth density, meaning a higher growth rate induces lower growth density and vice versa that follows a linear relationship. The highest growth rate found in the plot for Tetra lattices is more than 0.008 dt^{-1} for which the growth density is a bit more than 0.6, while the highest growth rate for BC-Tetra lattices is more than 0.02 dt^{-1} for which the growth density is a bit more than 0.4.

Fig. 15A shows that for the studied Tetra designs, high growth density-high growth rate is possible only with squashed lattices, all of the cubic and stretched designs have halted growth. This occurs because the squashed designs create smaller pore aspect ratios that enable pore bridging and sustained growth that is not achieved for the larger gaps in symmetrical and stretched structures. A lattice with Tetra unit cells highlighted from Fig. 15A represents a maximized growth rate scaffold that has a unit cell width of 550 μm and a height of 300 μm. A second lattice with unit cells width a width of 750 μm and a height of 350 μm represents a design with maximized growth density.

Fig. 15B shows that for the studied BC-Tetra designs, a high growth density-high growth rate region includes all three possible height adjustments: squashed, cubes, and stretched. The reason this occurs for BC-Tetra designs is due to the extra beams meeting in the center of each unit cell. The extra beams facilitate more localized curvature for sustained tissue growth in comparison to the void centers for the Tetra designs. The height adjustment makes it possible to tune the functionality trade-off of tissue growth rate and tissue growth density beyond the capabilities of the cubic unit cells that are traditionally considered when designing tissue scaffolds. Namely, the height adjustments of the Tetra cells lead to increase growth rate and growth density for squashed configurations, and BC-Tetra unit cells enable enhanced capabilities not possible from cubic unit cells when considering maximizing tissue growth rate or tissue growth density. Fig. 15B illustrates two lattices with BC-Tetra unit cells that are highlighted with capabilities beyond cubic configurations. The first lattice has squashed BC-Tetra unit cells with a width of 600 μm and a height of 500 μm that demonstrates a configuration with maximized growth rate, whereas the second lattice has stretched BC-Tetra unit cells with a width of 800 μm and a height of 1200 μm that demonstrates a design with maximized growth density. Overall, these results demonstrate the potential to tune lattice structures by altering unit cell width and height independently to achieve advanced capabilities that enable greater and improved optimal solutions for bone tissue engineering depending on the desired needs of a patient.

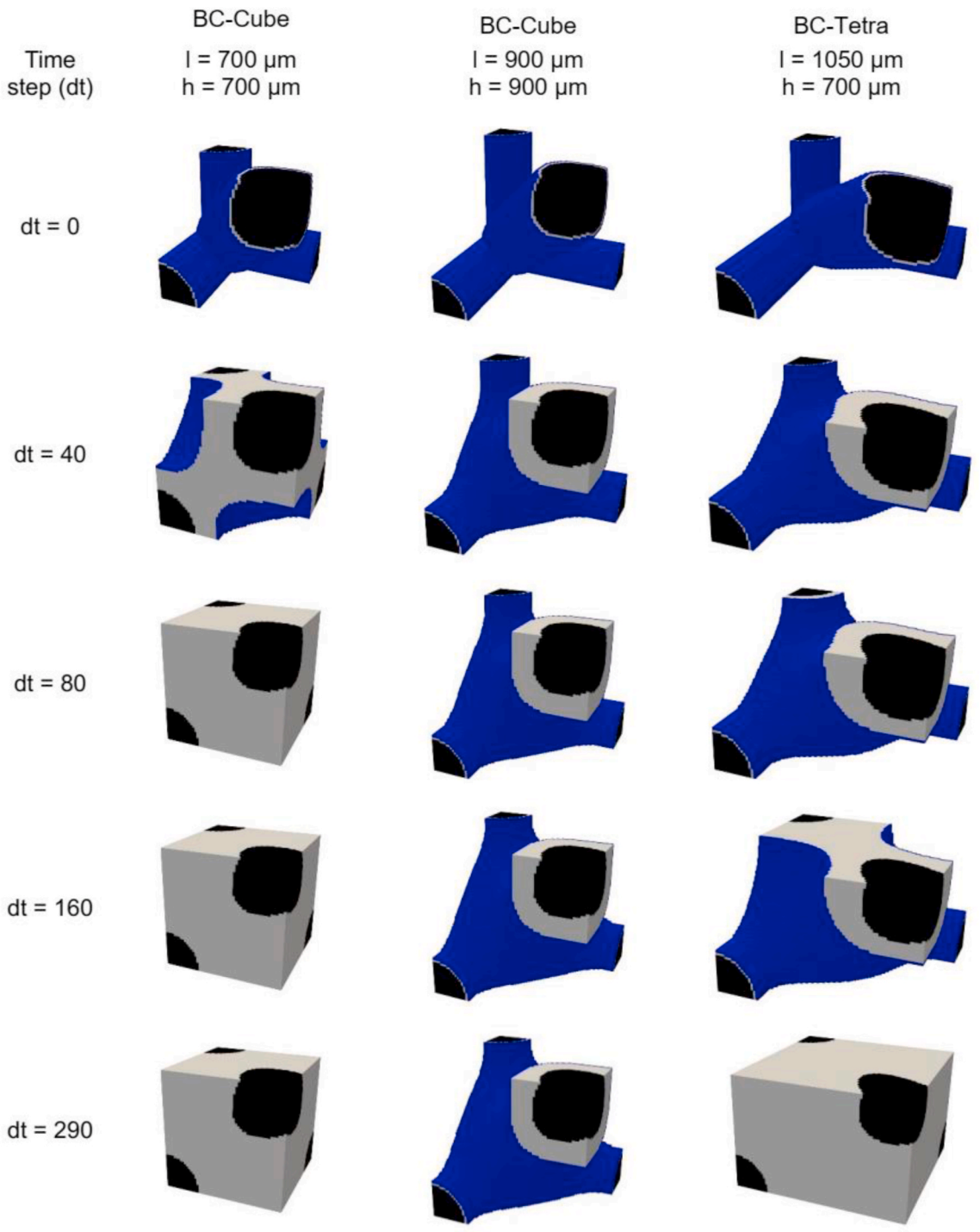

Fig. 10. Simulation rendering for tissue filling behavior of BC-Tetra lattices. Voxels represent structure (black), tissue (gray), interface (blue). Tissue voxels replace interface voxels with positive curvature each time step. Images exported from Paraview.

4. Discussion

Computational design exploration and evaluation were conducted when considering a class of Bravais lattices with tetragonal topologies for configuring bone tissue scaffolds studied through computational simulations. Investigations in tissue growth and mechanical stiffness demonstrated the benefits of stretching/squashing tetragonal unit cell structures to produce lattices with higher growth densities and directionally favorable elastic moduli in comparison to cubically symmetric designs. Design maps were generated to evaluate the tissue growth and mechanical properties of the tetragonal lattices through evaluating tissue growth density, tissue growth rate, and longitudinal/transverse elastic moduli. These maps enable the evaluation of a design space not previously explored, by considering complex lattices structures with multiple independent design parameters [48].

The design maps created in Fig. 6 demonstrate the porosity achieved by Tetra and BC-Tetra lattices with different height/width values, therefore enabling the identification of relevant configurations with porosities of 50%–80% suitable for bone tissue engineering. All lattices considered in the design map and throughout the study have a fixed beam diameter of 200 μm, which is achievable by printing with selective laser sintering that can achieve a minimum of 200 μm beam diameter

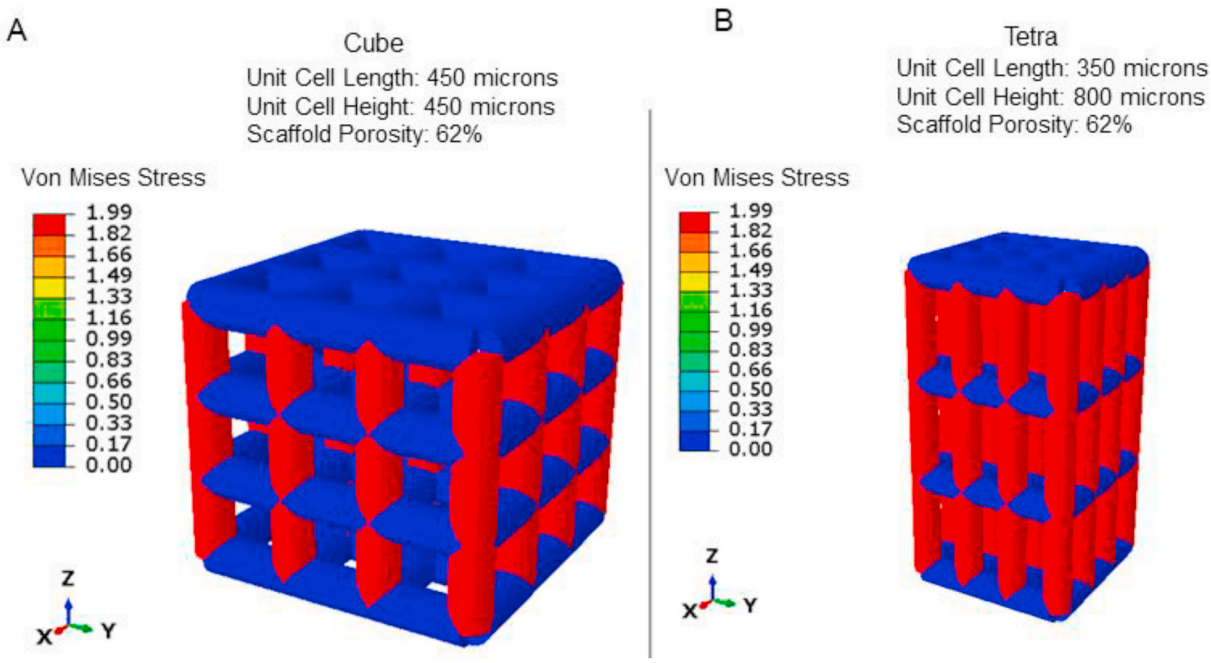

Fig. 11. Von Mises Stress for cubic Tetra and Tetra lattices. A) Cube structure with 62% porosity B) Tetra structure with 62% porosity. Von Mises Stress values depicted as color plots. Images exported from Abaqus.

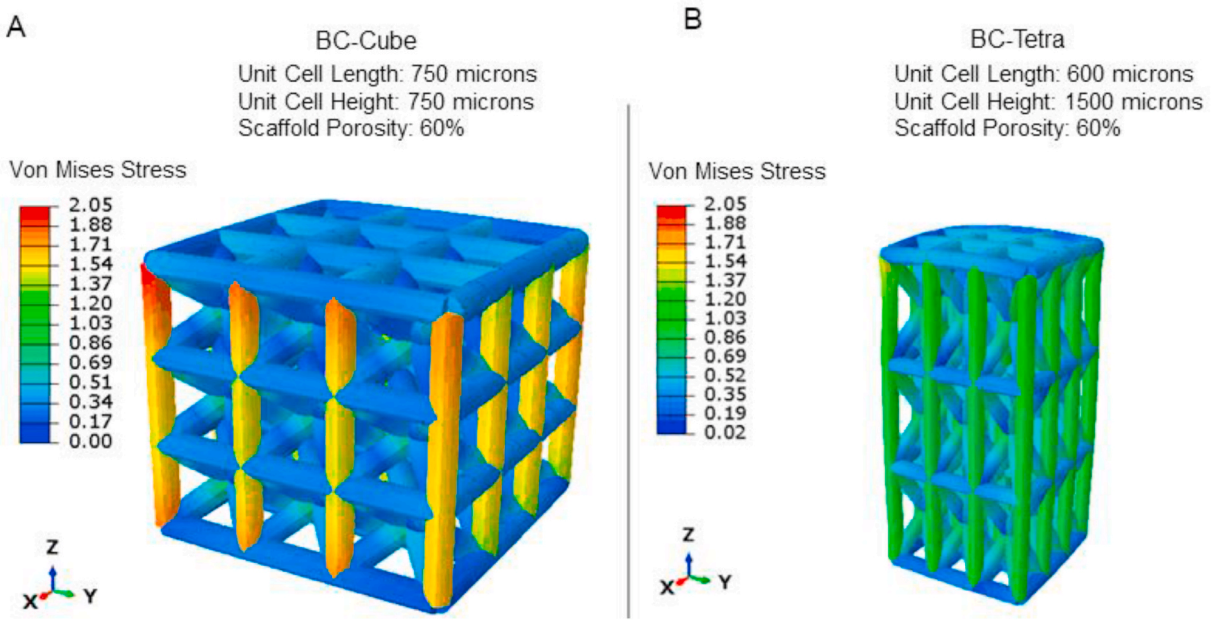

Fig. 12. Von Mises Stress for cubic BC-Tetra and BC-Tetra lattices. A) BC-Cube structure with 60% porosity B) BC-Tetra structure with 60% porosity. Von Mises Stress values are depicted as color plots. Images exported from Abaqus.

and possibly some stereolithography technologies [25,56]. Larger beam diameters have been considered for tissue scaffold lattices in the past, which are potentially easier to manufacture, however, when comparing tissue growth rates, generally lower beam diameters are preferred and in theory, a smaller beam size does not adversely affect mechanical performance if constructed with few printing defects [12].

Biology and mechanics simulations were investigated for selected unit cell configurations to determine how tissue growth and compression behavior differs for cubic and stretched/squashed Tetra and BC-Tetra unit cells. Biological simulations in Fig. 8 show that unit cells having no diagonal beam can avoid halted growth if tissue growth closes planar pores prior to halting since the grown tissue provide the later support for growth. Mechanical simulations in Figs. 11 and 12 demonstrate height adjustments do not affect the Von Mises Stress in lattices without diagonal beams but affect the Von Mises Stress with diagonal beams since the beam alignment changes for the diagonal beams.

Design maps in Figs. 13 and 14 demonstrate how tissue growth density, tissue growth rate, and elastic modulus change in scaffolds due to changes in unit cell parameters. The longitudinal elastic modulus is primarily dependent on the width of the Tetra lattices and is significantly influenced by the internal body-centered beam-alignment in the case of BC-Tetra lattices. Thus, the newly introduced design maps

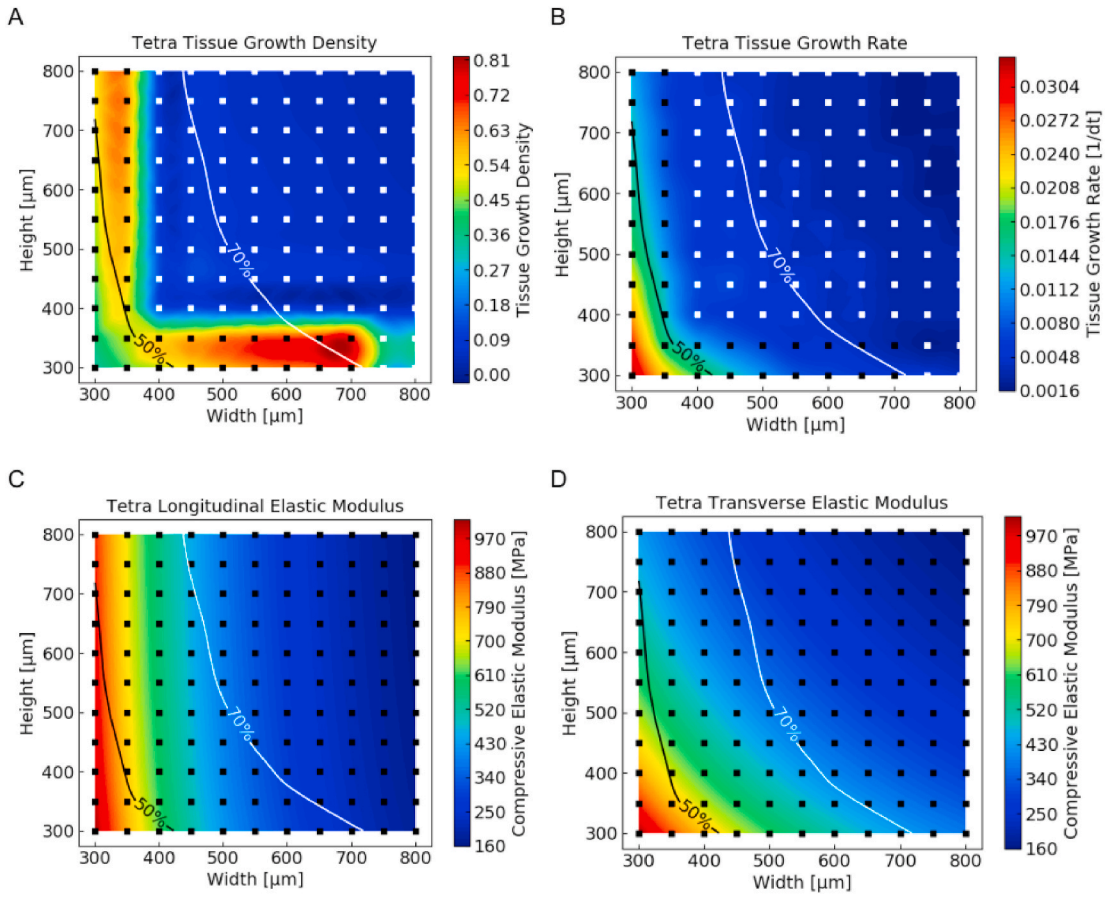

Fig. 13. Design maps for Tetra lattices. (A) Tissue growth density, (B) Tissue growth rate, (C) Longitudinal elastic modulus, (D) Transverse elastic modulus. Lines in the map indicate initial porosity of 50% and 70%, white dots indicate halted tissue growth, black dots indicate complete tissue growth. Dots represent the run simulations.

provide flexibility in selecting scaffolds from a wide range of tissue growth density, tissue growth rate, and elastic modulus property values and tunings. Design maps in Figs. 13 and 14 are in agreement with the literature on lattice behaviors. For instance, if initial porosity increases for the lattices with the same height and width, elastic modulus decreases, while tissue growth density increases until it reaches the halting behavior [12,57]. This is important from both biological and mechanical points of view. For instance, biologically a high tissue growth density is better for ensuring a large volume of tissue to promote biological activity such as mineralization, but a high tissue growth rate is important for amassing the tissue quickly for improved recovery speed. The elastic modulus of the scaffold should be the same or slightly less than the host bone tissue to confirm the load-carrying capability (too low of elastic modulus can cause inability to carry the load) and avoid stress shielding (too high of elastic modulus can cause stress shielding) [58]. Therefore, design maps are an important tool to provide flexibility to select fine-tuned scaffolds.

Fig. 15 demonstrates selected cases of unit cell parameters and how the selection of unit cell parameters can change the tissue growth density and tissue growth rate for a fixed elastic modulus relevant to bone tissue engineering. However, the ranges of tissue growth rates and elastic moduli that are preferable vary significantly depending on the bone type, defect type, and the host body. For instance, tibial defects naturally tend to recover in less time than calvarial defects and thus a higher tissue growth rate would facilitate a more natural course of recovery for tibial defects. Normally, the elastic modulus of human trabecular bone can range from 10 *MPa* to 3000 *MPa* [59]. Since bone is comprised of heterogeneous materials, elastic modulus varies even within a single bone structure [60]. Moreover, the host bone property of one patient is potentially drastically different from another patient and thus patient-specific scaffold design becomes more relevant [61]. Therefore, there is a need for continued adaption for the selection of scaffold design from design maps depending on the application. However, once design maps are created, they facilitate efficient optimization to find strong candidate designs that can be confirmed with more sophisticated mechanobiological simulations or experimental studies.

There are limitations in the study relevant to modeling assumptions, such as the mechanical finite element analysis using beam-based finite element models to ensure rapid relative comparisons of the bulk data obtained. Solid modeling could improve accuracy in addition to simulating print defects once viable candidate designs are narrowed down from the bulk analysis. The biological simulation uses a voxel environment that is subject to numerical rounding errors since curvature is calculated based on discrete voxels. An ideal scanning mask for calculating curvature should approximate a continuous sphere, however, this results in longer computational time so a scanning mask size with an acceptable numerical error was selected based on past studies [31,62]. These assumptions are also in line with the *in vivo* and *in vitro* experiments suggesting one day in culture is equal to about 12 time steps in the simulation [46]. Further improvements in biological modeling could include simulating fluid shear stress, vascularization, and nutrient transport phenomena to improve fidelity. However, the strength of the currently used computational approach is an investigation of diverse candidate geometries that are enabled by 3D printing which creates an immense design space. Based on the design space size, it is more appropriate to map many candidate designs with computationally efficient methods to identify favorable designs before fine-tuning the structural configuration based on more computationally expensive

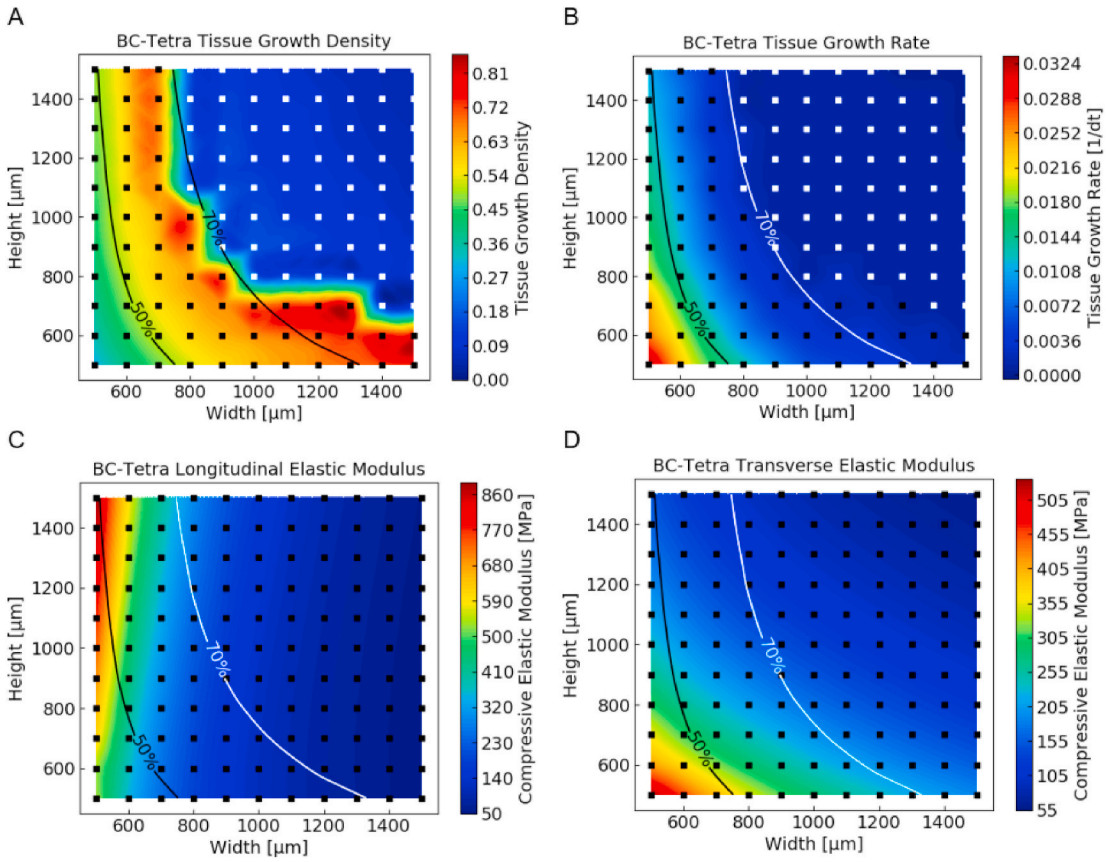

Fig. 14. Design maps for BC-Tetra lattices. (A)Tissue growth density, (B) Tissue growth rate, (C) Longitudinal elastic modulus, (D) Transverse elastic modulus. Lines in the map indicate initial porosity (50% and 70%), white dots indicate halted tissue growth, black dots indicate complete tissue growth (A and B). Dots represent the run simulations.

evaluations.

There are several areas where future work could build upon these studies as more computationally efficient methodologies are developed with further experimentation. For instance, nutrient availability plays a significant role in tissue growth but is exceedingly complex to compute due to the need to consider fluid transport, nutrient use by tissue, and vascularization. Generally, reduced nutrient availability is hypothesized to result in slowed or halted growth, generally towards the center of the scaffold where nutrients are least available [63]. Thereby meaning the growth behavior of the tissue adheres to curvature-based growth but is adjusted in terms of rate, especially when considering larger scaffolds. Generally, it is assumed the boundary layers of a scaffold would receive more nutrients than inner layers, which has motivated hierarchical design approaches to ensure sufficient tissue growth throughout the scaffold [50,64]. Future computational approaches could consider updating growth rates based on nutrient availability if interfaced with iterative evaluation approaches that compute the exact nutrients available spatially throughout the scaffold during each time step and adjust growth patterns accordingly. However, such an approach would require vastly more computational resources making the bulk analysis conducted in this paper impractical. When considering the full scaffold, it is possible to make adjustments by implementing more complete computational fluid dynamic environments [40], approximating permeability with the Kozeny-Carmen model [25], or considering design approaches that ensure complete nutrition availability such as pre-vascularization [65].

The tissue growth simulations were conducted independently from mechanical stiffness assessments to facilitate bulk analysis and computational efficiency to compare many scaffold designs and focus on the growth of tissue in relation to the topological design of the scaffold. It is predicted that mechanical loads may result in increased tissue growth rates [66], however, the strain experienced by the tissue growing in the scaffolds that may alter their behavior in this study is very low. For instance, in a scaffold of 300 MPa experiencing a 1 kN loading typical of the spine [67], the strain is only 0.008 when a scaffold has 1 cm height and 2 cm width, which results in less than 1% displacement of unit cells in the scaffold under load. Such a low strain results in nearly no displacement of the scaffold, yet retains the effective elastic modulus and stiffness necessary to match trabecular bone's properties and mitigate mechanical failure.

Since this study considers polymeric biodegradable materials for mechanical property assessment, such as polylactic acid, methacrylic acid, or polycaprolactone materials, it is assumed the materials will eventually degrade over time. Previous studies have demonstrated that the degradation rate of these polymers generally requires several years, which is much slower than the expected rate of bone growth to replace the scaffold material [68,69]. The tissue growth time calculated for the Tetra and BC-Tetra structures is generally several months-long prior to convergence, which is much faster than the degradation rate. It is assumed these structures have minimal swelling, which is in agreement with previous studies investigating polymer 3D printing materials while the degradation rate occurs proportional to surface-area to volume ratio for the structure [23,64].

Overall this research suggests that height-adjusted tetragonal unit cells achieve higher tissue growth density than non-height-adjusted structures of similar porosity. Although the higher tissue growth density comes with trade-offs, such as lower tissue growth rate or variances in elastic moduli, the investigation of this new portion of the design space opens enormous design possibilities of finding even better characteristics through continued investigations. Future work may carry out

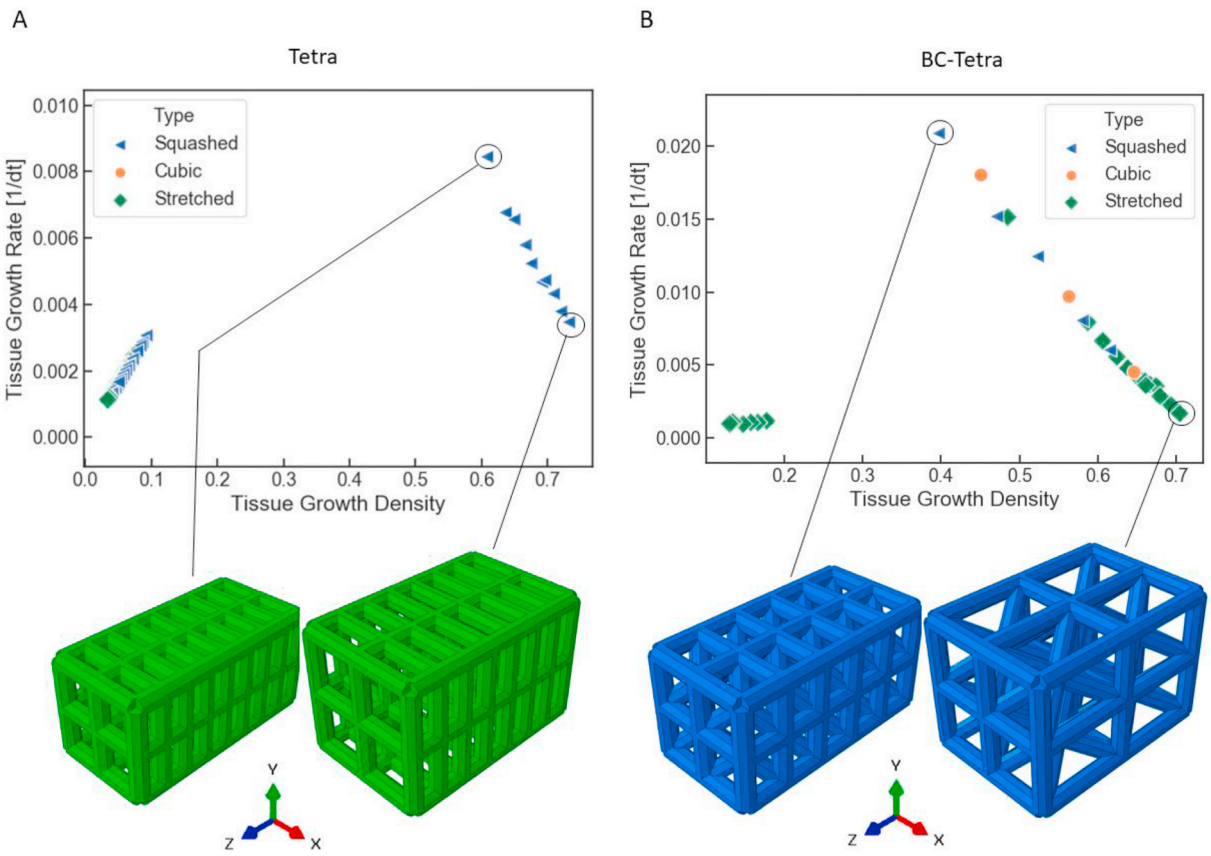

Fig. 15. Growth Rate and Growth Density comparisons. Scaffold designs are compared for lattices with A) Tetra or B) BC-Tetra unit cells. All data points for scaffolds have longitudinal elastic modulus in the range of 200 MPa–400 MPa. Selected scaffolds demonsrate high tissue growth rate or tissue growth density designs. Structural design images exported from Abaqus.

computational investigations for assessing further nutrient transport, mechanobiological behaviors, or degradation phenomena for a more detailed assessment of biological growth in relation to scaffold design, while there are also many opportunities for further exploring topologies, materials, and scaffold layouts using computational methodologies to efficiently generate and assess bulk scaffold designs.

5. Conclusion

This study conducted a computational investigation of tetragonal lattices designed for tissue engineering applications with evaluations of biological and mechanical functionality and compared tetragonal lattices designed with non-equal height and width to cubic lattices with equal height and width as controls. The study demonstrated tetragonal lattices have higher tissue growth density than cubic lattices of similar porosity and can achieve advantageous elastic moduli in preferred loading directions. The biaxial parametric independence in unit cell design allows more flexibility for designing scaffolds with favorable mechanical and biological properties. These findings aid in configuring fine-tuned tissue scaffold designs through careful consideration of the biological and mechanical scaffold functionality, which is a crucial step in developing optimized solutions in personalized medicine.

Declaration of competing interest

The authors declare that they have no known competing financial interests or personal relationships that could have appeared to influence the work reported in this paper.

Acknowledgement

An earlier iteration of this study was published in the 2020 ASME Design Automation Conference [70].

References

[1] A. Kantaros, N. Chatzidai, D. Karalekas, 3D printing-assisted design of scaffold structures, Int. J. Adv. Manuf. Technol. 82 (1–4) (2015) 559–571, https://doi.org/10.1007/s00170-015-7386-6.
[2] R. Lam, W. Chen, Biomedical Devices: Materials, Design and Manufacturing, Springer Nature, 2019.
[3] A. Souness, F. Zamboni, G.M. Walker, M.N. Collins, Influence of scaffold design on 3D printed cell constructs, J. Biomed. Mater. Res. B Appl. Biomater. 106 (2) (2018) 533–545, https://doi.org/10.1002/jbm.b.33863. Feb.
[4] P.F. Egan, Integrated design approaches for 3D printed tissue scaffolds: review and outlook, Materials 12 (15) (2019) 2355.
[5] D. Durdevic, et al., A novel autologous bone graft substitute comprised of rhBMP6 blood coagulum as carrier tested in a randomized and controlled Phase I trial in patients with distal radial fractures, Bone 140 (2020) 115551, https://doi.org/10.1016/j.bone.2020.115551. Nov.
[6] S.J. Hollister, Scaffold design and manufacturing: from concept to clinic, Adv. Mater. 21 (32–33) (2009) 3330–3342, https://doi.org/10.1002/adma.200802977. Sep. 4.
[7] C. Torres-Sanchez, F.R.A. Al Mushref, M. Norrito, K. Yendall, Y. Liu, P.P. Conway, The effect of pore size and porosity on mechanical properties and biological response of porous titanium scaffolds, Mater. Sci. Eng. C Mater. Biol. Appl. 77 (2017) 219–228, https://doi.org/10.1016/j.msec.2017.03.249. Aug 1.
[8] S.M. Ahmadi, et al., Mechanical behavior of regular open-cell porous biomaterials made of diamond lattice unit cells, J. Mech. Behav. Biomed. Mater. 34 (2014) 106–115, https://doi.org/10.1016/j.jmbbm.2014.02.003. Jun.
[9] M. Campolo, F. Curcio, A. Soldati, Minimal perfusion flow for osteogenic growth of mesenchymal stem cells on lattice scaffolds, AIChE J. 59 (8) (2013) 3131–3144, https://doi.org/10.1002/aic.14084.
[10] Y. Du, et al., Finite element analysis of mechanical behavior, permeability of irregular porous scaffolds and lattice-based porous scaffolds, Mater. Res. Express 6 (10) (2019), https://doi.org/10.1088/2053-1591/ab3ac1.

[11] P. Egan, Design and Biological Simulation of 3d Printed Lattices for Biomedical Applications, ASME IDETC, 2019 presented at the.

[12] P.F. Egan, K.A. Shea, S.J. Ferguson, Simulated tissue growth for 3D printed scaffolds, Biomech. Model. Mechanobiol. 17 (5) (2018) 1481–1495, https://doi.org/10.1007/s10237-018-1040-9. Oct.

[13] F. Liu, D.Z. Zhang, P. Zhang, M. Zhao, S. Jafar, Mechanical properties of optimized diamond lattice structure for bone scaffolds fabricated via selective laser melting, Materials 11 (3) (2018), https://doi.org/10.3390/ma11030374. Mar 3.

[14] A.A. Zadpoor, Bone tissue regeneration: the role of scaffold geometry, Biomater. Sci. 3 (2014).

[15] D.A. Garzón-Alvarado, Y. Lancheros, M.A. Velasco, Geometric and mechanical properties evaluation of scaffolds for bone tissue applications designing by a reaction-diffusion models and manufactured with a material jetting system, J. Comput. Desig. Eng. 3 (4) (2016) 385–397, https://doi.org/10.1016/j.jcde.2016.06.006.

[16] F. Guilak, D.L. Butler, S.A. Goldstein, F.P. Baaijens, Biomechanics and mechanobiology in functional tissue engineering, J. Biomech. 47 (9) (2014) 1933–1940, https://doi.org/10.1016/j.jbiomech.2014.04.019. Jun 27.

[17] K. Ono, K. Ohmori, T. Hori, Clinical and radiological outcomes of corrective surgery on adult spinal deformity patients: comparison of short and long fusion, Adv. Orthoped. 2019 (2019). https://www.hindawi.com/journals/aorth/2019/9492486/.

[18] M. Manzur, et al., The rate of fusion for stand-alone anterior lumbar interbody fusion: a systematic review, Spine J. (2019).

[19] P. Li, et al., A novel 3D printed cage with microporous structure and in vivo fusion function, J. Biomed. Mater. Res. (2019).

[20] H. Kang, S.J. Hollister, F. La Marca, P. Park, C.-Y. Lin, Porous biodegradable lumbar interbody fusion cage design and fabrication using integrated global-local topology optimization with laser sintering, J. Biomech. Eng. 135 (10) (2013) 101013.

[21] H. Kolken, et al., Additively manufactured space-filling meta-implants, Acta Biomater. 125 (2021) 345–357.

[22] M.A. Plantz, et al., Osteoinductivity and biomechanical assessment of a 3D printed demineralized bone matrix-ceramic composite in a rat spine fusion model, Acta Biomater. 127 (2021) 146–158.

[23] P.F. Egan, I. Bauer, K. Shea, S.J. Ferguson, Mechanics of three-dimensional printed lattices for biomedical devices, J. Mech. Des. 141 (3) (2019), 031703.

[24] T.A. Schaedler, W.B. Carter, Architected cellular materials, Annu. Rev. Mater. Res. 46 (1) (2016) 187–210, https://doi.org/10.1146/annurev-matsci-070115-031624.

[25] P.F. Egan, V.C. Gonella, M. Engensperger, S.J. Ferguson, K. Shea, Computationally designed lattices with tuned properties for tissue engineering using 3D printing, PLoS One 12 (8) (2017), e0182902, https://doi.org/10.1371/journal.pone.0182902.

[26] V. Rati, N. Singh, S. Rai, S. Kumta, Triply periodic minimal surface-based porous scaffold design and analysis subjected to hard tissue reconstruction, in: Presented at the Advances in Computational Methods in Manufacturing, Lecture Notes on Multidisciplinary Industrial Engineering, 2019.

[27] S. Sturm, S. Zhou, Y.W. Mai, Q. Li, On stiffness of scaffolds for bone tissue engineering-a numerical study, J. Biomech. 43 (9) (2010) 1738–1744, https://doi.org/10.1016/j.jbiomech.2010.02.020. Jun 18.

[28] D. Hutmacher, Scaffold design and fabrication technologies for engineering tissues — state of the art and future perspectives, J. Biomater. Sci. Polym. Ed. 12 (1) (2001) 107–124.

[29] A.A. Al-Tamimi, P.R.A. Fernandes, C. Peach, G. Cooper, C. Diver, P.J. Bartolo, Metallic bone fixation implants: a novel design approach for reducing the stress shielding phenomenon, Virtual Phys. Prototyp. 12 (2) (2017) 141–151, https://doi.org/10.1080/17452759.2017.1307769.

[30] D.P. Byrne, D. Lacroix, J.A. Planell, D.J. Kelly, P.J. Prendergast, Simulation of tissue differentiation in a scaffold as a function of porosity, Young's modulus and dissolution rate: application of mechanobiological models in tissue engineering, Biomaterials 28 (36) (2007) 5544–5554.

[31] S. Checa, P.J. Prendergast, Effect of cell seeding and mechanical loading on vascularization and tissue formation inside a scaffold: a mechano-biological model using a lattice approach to simulate cell activity, J. Biomech. 43 (5) (2010) 961–968, https://doi.org/10.1016/j.jbiomech.2009.10.044. Mar 22.

[32] M. Dias, P. Fernandes, J. Guedes, S. Hollister, Permeability analysis of scaffolds for bone tissue engineering, J. Biomech. 45 (6) (2012) 938–944.

[33] P. Joly, et al., Geometry-driven cell organization determines tissue growths in scaffold pores: consequences for fibronectin organization, PLoS One 8 (9) (2013), e73545.

[34] M. Rumpler, A. Woesz, J.W. Dunlop, J.T. van Dongen, P. Fratzl, The effect of geometry on three-dimensional tissue growth, J. R. Soc. Interface 5 (27) (2008) 1173–1180.

[35] S. Ehrig, et al., Surface tension determines tissue shape and growth kinetics, Sci. Adv. 5 (9) (2019), https://doi.org/10.1126/sciadv.aav9394.

[36] M. Paris, et al., Scaffold curvature-mediated novel biomineralization process originates a continuous soft tissue-to-bone interface, Acta Biomater. 60 (2017) 64–80, https://doi.org/10.1016/j.actbio.2017.07.029. Sep. 15.

[37] A. Boccaccio, A.E. Uva, M. Fiorentino, L. Lamberti, G. Monno, A mechanobiology-based algorithm to optimize the microstructure geometry of bone tissue scaffolds, Int. J. Biol. Sci. 12 (1) (2016) 1.

[38] K. Garikipati, A continuum treatment of growth in biological tissue: the coupling of mass transport and mechanics, J. Mech. Phys. Solid. 52 (7) (2004) 1595–1625, https://doi.org/10.1016/j.jmps.2004.01.004.

[39] P. Van Liedekerke, M.M. Palm, N. Jagiella, D. Drasdo, Simulating tissue mechanics with agent-based models: concepts, perspectives and some novel results, Comput. Part. Mech. 2 (4) (2015) 401–444, https://doi.org/10.1007/s40571-015-0082-3.

[40] Y. Guyot, I. Papantoniou, F.P. Luyten, L. Geris, Coupling curvature-dependent and shear stress-stimulated neotissue growth in dynamic bioreactor cultures: a 3D computational model of a complete scaffold, Biomech. Model. Mechanobiol. 15 (1) (2016) 169–180, https://doi.org/10.1007/s10237-015-0753-2. Feb.

[41] H.G. Lee, J. Park, S. Yoon, C. Lee, J. Kim, Mathematical model and numerical simulation for tissue growth on bioscaffolds, Appl. Sci. 9 (2019) 19, https://doi.org/10.3390/app9194058.

[42] U. Stachewicz, P.K. Szewczyk, A. Kruk, A.H. Barber, A. Czyrska-Filemonowicz, Pore shape and size dependence on cell growth into electrospun fiber scaffolds for tissue engineering: 2D and 3D analyses using SEM and FIB-SEM tomography, Mater. Sci. Eng. C Mater. Biol. Appl. 95 (2019) 397–408, https://doi.org/10.1016/j.msec.2017.08.076. Feb 1.

[43] S.J. Callens, R.J. Uyttendaele, L.E. Fratila-Apachitei, A.A. Zadpoor, Substrate curvature as a cue to guide spatiotemporal cell and tissue organization, Biomaterials 232 (2020) 119739.

[44] C.M. Bidan, et al., How linear tension converts to curvature: geometric control of bone tissue growth, PLoS One 7 (5) (2012), e36336.

[45] C.M. Bidan, F.M. Wang, J.W. Dunlop, A three-dimensional model for tissue deposition on complex surfaces, Comput. Methods Biomech. Biomed. Eng. 16 (10) (2013) 1056–1070.

[46] C.M. Bidan, K.P. Kommareddy, M. Rumpler, P. Kollmannsberger, P. Fratzl, J. W. Dunlop, Geometry as a factor for tissue growth: towards shape optimization of tissue engineering scaffolds, Adv. Healthcare Mater. 2 (1) (2013) 186–194.

[47] Y. Guyot, I. Papantoniou, Y.C. Chai, S. Van Bael, J. Schrooten, L. Geris, A computational model for cell/ECM growth on 3D surfaces using the level set method: a bone tissue engineering case study, Biomech. Model. Mechanobiol. 13 (6) (2014) 1361–1371.

[48] S. Arabnejad, R. Burnett Johnston, J.A. Pura, B. Singh, M. Tanzer, D. Pasini, High-strength porous biomaterials for bone replacement: a strategy to assess the interplay between cell morphology, mechanical properties, bone ingrowth and manufacturing constraints, Acta Biomater. 30 (2016) 345–356, https://doi.org/10.1016/j.actbio.2015.10.048. Jan.

[49] D. Melancon, Z.S. Bagheri, R.B. Johnston, L. Liu, M. Tanzer, D. Pasini, Mechanical characterization of structurally porous biomaterials built via additive manufacturing: experiments, predictive models, and design maps for load-bearing bone replacement implants, Acta Biomater. 63 (2017) 350–368, https://doi.org/10.1016/j.actbio.2017.09.013. Nov.

[50] M. Moniruzzaman, C. O'Neal, A. Bhuiyan, P.F. Egan, Design and mechanical testing of 3D printed hierarchical lattices using biocompatible stereolithography, Design 4 (3) (2020) 22.

[51] S.I. Roohani-Esfahani, P. Newman, H. Zreiqat, Design and fabrication of 3D printed scaffolds with a mechanical strength comparable to cortical bone to repair large bone defects, Sci. Rep. 6 (2016) 19468, https://doi.org/10.1038/srep19468. Jan 19.

[52] H. Tiainen, S.P. Lyngstadaas, J.E. Ellingsen, H.J. Haugen, Ultra-porous titanium oxide scaffold with high compressive strength, J. Mater. Sci. Mater. Med. 21 (10) (2010) 2783–2792, https://doi.org/10.1007/s10856-010-4142-1. Oct.

[53] G. Briguiet, P. Egan, Structure, Process and Material Influences for 3d Printed Lattices Designed with Mixed Unit Cells, ASME IDETC, 2020 presented at the.

[54] A.M.E. Arefin, N.R. Khatri, N. Kulkarni, P.F. Egan, Polymer 3D printing review: materials, process, and design strategies for medical applications, Polymers 13 (9) (2021), https://doi.org/10.3390/polym13091499. May 6.

[55] A.R. Amini, C.T. Laurencin, S.P. Nukavarapu, Bone tissue engineering: recent advances and challenges, Crit. Rev. Biomed. Eng. 40 (5) (2012) 363–408.

[56] S.A. Skoog, P.L. Goering, R.J. Narayan, Stereolithography in tissue engineering, J. Mater. Sci. Mater. Med. 25 (3) (2014) 845–856, https://doi.org/10.1007/s10856-013-5107-y. Mar.

[57] P. Pandithevan, G.S. Kumar, Finite element analysis of a personalized femoral scaffold with designed microarchitecture, Proc. Inst. Mech. Eng. H 224 (7) (2010) 877–889, https://doi.org/10.1243/09544119JEIM633.

[58] J. Lim, J. Lee, H.-S. Yun, H.-I. Shin, E.K. Park, Comparison of bone regeneration rate in flat and long bone defects: calvarial and tibial bone, Tissue Eng. Regener. Med. 10 (6) (2013) 336–340, https://doi.org/10.1007/s13770-013-1094-9.

[59] E.F. Morgan, G.U. Unnikrisnan, A.I. Hussein, Bone mechanical properties in healthy and diseased states, Annu. Rev. Biomed. Eng. 20 (2018) 119–143, https://doi.org/10.1146/annurev-bioeng-062117-121139. Jun 4.

[60] I.F. Cengiz, et al., Building the basis for patient-specific meniscal scaffolds: from human knee MRI to fabrication of 3D printed scaffolds, Bioprinting 1–2 (2016) 1–10, https://doi.org/10.1016/j.bprint.2016.05.001.

[61] S. Scheiner, C. Hellmich, Patient-specific design of tissue engineering scaffolds, based on mathematical modeling, Adv. Ceram. Biomater. (2017) 391–406.

[62] M.S. Hossain, D.J. Bergstrom, X.B. Chen, Computational modelling of the scaffold-free chondrocyte regeneration: a two-way coupling between the cell growth and local fluid flow and nutrient concentration, Biomech. Model. Mechanobiol. 14 (6) (2015) 1217–1225, https://doi.org/10.1007/s10237-015-0666-0. Nov.

[63] J.R. Vetsch, R. Müller, S. Hofmann, The evolution of simulation techniques for dynamic bone tissue engineering in bioreactors, J. Tiss. Eng. Regener. Med. 9 (8) (2013).

[64] P. Egan, S. Ferguson, K. Shea, Design of hierarchical 3D printed scaffolds considering mechanical and biological factors for bone tissue engineering, J. Mech. Des. 139 (6) (2017).

[65] H.G. Song, R.T. Rumma, C.K. Ozaki, E.R. Edelman, C.S. Chen, Vascular tissue engineering: progress, challenges, and clinical promise, Cell Stem Cell 22 (3) (2018) 340–354, https://doi.org/10.1016/j.stem.2018.02.009. Mar 1.

[66] Ó.L. Rodríguez-Montaño, et al., Comparison of the mechanobiological performance of bone tissue scaffolds based on different unit cell geometries, J. Mech. Behav. Biomed. Mater. 83 (2018) 28–45.

[67] P. Egan, X. Wang, H. Greutert, K. Shea, K. Wuertz-Kozak, S. Ferguson, Mechanical and Biological Characterization of 3D Printed Lattices, 3D Printing and Additive Manufacturing, 2019.

[68] R. Dwivedi, et al., Polycaprolactone as biomaterial for bone scaffolds: review of literature, J. Oral Biol. Craniofac Res. 10 (1) (2020) 381–388, https://doi.org/10.1016/j.jobcr.2019.10.003. Jan-Mar.

[69] K. Kim, et al., Control of degradation rate and hydrophilicity in electrospun non-woven poly(d,l-lactide) nanofiber scaffolds for biomedical applications, Biomaterials 24 (27) (2003) 4977–4985, https://doi.org/10.1016/s0142-9612(03)00407-1.

[70] A. Arefin, P. Egan, Computational Design Generation and Evaluation of Beam Based Tetragonal Bravais Lattice Structures for Tissue Engineering, ASME IDETC, 2020.